Construction of the Remote Sensing Systems V3.2 Atmospheric Temperature Records from the MSU and AMSU Microwave Sounders

CARL A. MEARS AND FRANK J. WENTZ

Remote Sensing Systems, Santa Rosa, California

(Manuscript received 21 May 2008, in final form 8 October 2008)

ABSTRACT

Measurements made by microwave sounding instruments provide a multidecadal record of atmospheric temperature change. Measurements began in late 1978 with the launch of the first Microwave Sounding Unit (MSU) and continue to the present. In 1998, the first of the follow-on series of instruments—the Advanced Microwave Sounding Units (AMSUs)—was launched. To continue the atmospheric temperature record past 2004, when measurements from the last MSU instrument degraded in quality, AMSU and MSU measurements must be intercalibrated and combined to extend the atmospheric temperature data records. Calibration methods are described for three MSU–AMSU channels that measure the temperature of thick layers of the atmosphere centered in the middle troposphere, near the tropopause, and in the lower stratosphere. Some features of the resulting datasets are briefly summarized.

1. Introduction

Temperature sounding microwave radiometers flown on polar-orbiting weather satellites provide an important record of upper-atmosphere temperatures, beginning with the Microwave Sounding Unit (MSU) on the Television and Infrared Observation Satellite (*TIROS-N*) in late 1978. In the following years, a series of eight additional MSU instruments provided a continuous record up to the present, with the MSU on *National Oceanic and Atmospheric Administration Satellite 14* (*NOAA-14*) still in operation. The MSU instruments made sounding measurements using four channels. Thermal emission from atmospheric oxygen constitutes the major component of the measured brightness temperature, with the maximum in the vertical weighting profile varying from near the surface in channel 1 to the lower stratosphere in channel 4. Channels 2, 3, and 4, which measure thick layers of the atmosphere centered in the middle troposphere, near the tropopause, and in the lower stratosphere, respectively, are relatively free of complicating effects of surface emission, clouds, and water vapor. Of these, only channels 2 and 4 have continuous data over the entire period of observation. Channel 3 contains substantial errors in the *NOAA-6* and *NOAA-9* instruments and thus is only valid from 1987 onward. Although the MSU data suffer from a number of calibration issues and time-varying biases, several groups, including our own, have merged the data from these nine instruments together into a single climate quality data record (Christy et al. 2000, 2003; Grody et al. 2004; Mears et al. 2003; Prabhakara et al. 2000; Vinnikov et al. 2005; Zou et al. 2006). It is important to continue this record into the future to ensure the existence of a high-quality record of atmospheric temperatures for climate change detection and climate model verification activities. The data continuity from the last MSU instrument, operating on the *NOAA-14* platform, began to degrade significantly after December 2004 when large gaps became common in the data. A follow-on series of instruments, the Advanced Microwave Sounding Units (AMSUs) began operation in mid-1998. The AMSU instruments have a larger set of observation frequencies, three of which are fairly well matched to the MSU channels 2, 3, and 4.

In this paper, we describe the procedures we have used to merge data from the newer AMSU instruments with data from the earlier MSU instruments. This merging procedure is complicated by 1) the slightly different observation frequencies and bandwidths used by the two instruments that lead to slightly different weighting functions for the same viewing geometry and 2) the discovery

Corresponding author address: Carl A. Mears, Remote Sensing Systems, 438 First Street, Suite 200, Santa Rosa, CA 95401.
E-mail: mears@remss.com

DOI: 10.1175/2008JTECHA1176.1

of spurious trends in the differences between satellite pairs during the period of AMSU operation. In section 2, we provide more details about the two instruments, focusing on their differences. In section 3, we describe the spurious trends we find in the differences for AMSU channels 5 through 9 between measurements made by the *NOAA-15* and *NOAA-16* satellites and argue that *NOAA-16* is the source of these trends. In section 4, we describe the method we have used to merge measurements from MSU channels 2, 3, and 4 with measurements from the corresponding AMSU channels 5, 7, and 9. In section 5, we present the results of our procedures. This paper does not describe uncertainty estimates in these datasets or the lower tropospheric temperature (TLT) datasets constructed by extrapolating MSU2 and AMSU5 lower in the atmosphere (Christy et al. 2003; Mears and Wentz 2005; Spencer and Christy 1992). These topics will be addressed in upcoming papers.

2. Description of the MSU and AMSU instruments

a. Swath geometry

Both MSU and AMSU are cross-track scanning radiometers that measure the upwelling brightness temperature at different view angles as they scan the earth perpendicular to the satellite subtrack. They are both ''step and integrate'' instruments that move a scanning mirror to a new position and then make an averaged radiance measurement over a fixed integration time. After making a measurement at each earth viewing position, a two-point calibration is performed by rotating the mirror to view cold space and then a calibration target whose unregulated temperature is monitored with multiple precision thermistors. MSU views the earth at 11 view angles separated by 9.47°, yielding a range of view angles from 0.0° for the nadir view to 47.35° for the two views farthest from nadir (Kidwell 1998). Each scan, including the two calibration measurements, takes 25.6 s. On the earth's surface, this corresponds to earth incidence angles ranging from 0.0° to approximately 56.19°. MSU has a half-power beamwidth of 7.5°, corresponding to a nadir spot size on the earth of 110 km × 110 km, expanding to 178 km × 322 km for the near-limb view due both to the increased distance from the spacecraft and to the oblique earth incidence angle. The AMSU instruments have significantly higher spatial resolution, viewing the earth at 30 viewing angles separated by 3.33°, with view angles ranging from 1.67° to 48.33° (Goodrum et al. 2000). Each scan takes 8 s. The view angles correspond to earth incidence angles ranging from 1.88° to 57.22°. The half-power beamwidth of the AMSU instrument is 3.3°, yielding a nadir spot size of 48 km × 48 km, expanding to 80 km × 150 km for the near-limb views. Our existing MSU2 dataset is an average of the central five MSU views, giving a swath width of approximately 640 km. For AMSU5 and AMSU7, we choose to use the central 12 fields of view (views 10–21), yielding a swath width of approximately 660 km, close to the MSU swath width for the central five views, thus keeping the spatial sampling similar to that for MSU. For AMSU9, differences in the measurement frequency made it necessary to use a set of eight views (views 7–10 and 21–24) with larger incidence angles, resulting in a wider measurement swath with a stripe missing from its center. The choice of field of view for each AMSU channel is discussed in more detail in sections 2b and 4c below.

b. Temperature weighting functions

By choosing measurement frequencies where the atmosphere is (almost) opaque, the upwelling radiation measured by microwave sounders is representative of the temperature of thick layers of the earth's atmosphere. We use a temperature weighting function to describe the relative contribution of each atmospheric layer to the observed brightness temperature T_b:

$$T_b = W_S T(0) + \int_0^{\mathrm{TOA}} W(z)T(z)dz, \tag{1}$$

where W_s is the surface weight, $T(z)$ is the temperature at height z, and $W(z)$ is the temperature weighting function, and the integral extends from the surface to the top of the atmosphere (TOA). The surface weight and the temperature weighting functions are dependent on the atmospheric absorption coefficient $\kappa(z)$ as a function of height z, the surface emissivity e_s, and the earth incidence angle θ (Ulaby et al. 1981). The surface weight is given by the product of e_s and the attenuation from the surface to the top of the atmosphere:

$$W_s = e_s e^{-\tau(0,\infty)\sec\theta}, \tag{2}$$

where

$$\tau(z_1, z_2) = \int_{z_1}^{z_2} \kappa(z)dz \tag{3}$$

is the zenith optical depth for a layer that extends in height from z_1 to z_2, with $z_2 = \infty$ representing the top of the atmosphere. The weighting function is given by

$$W(z) = \kappa(z)\sec\theta e^{-\tau(z,\infty)\sec\theta} + \kappa(z)\sec\theta e^{-\tau(0,z)\sec\theta}(1 - e_s)e^{-\tau(0,\infty)\sec\theta}. \tag{4}$$

The first term is due to radiation emitted in the upward direction attenuated by the absorption of the intervening

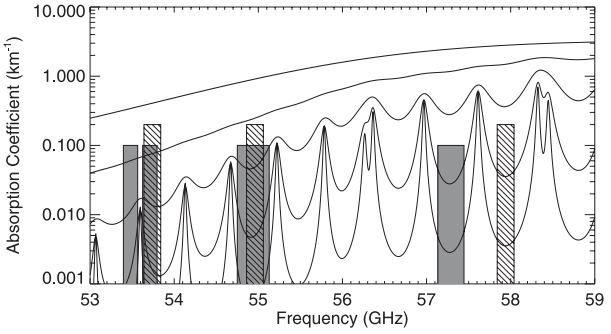

FIG. 1. The lines show the absorption coefficient as a function of frequency for five representative pressures: 1000 (highest line), 300, 100, 30, and 10 hPa (lowest line). At high pressure, the individual absorption lines merge into a single broad line because of pressure broadening, whereas at low pressure the individual lines are still distinct, making the bandwidth of each measurement band important. The rectangles show the MSU (filled with diagonal lines) and AMSU (gray) measurement bands for the channels described in the text. (The height of the rectangles has no meaning; it serves to help separate the bands visually.)

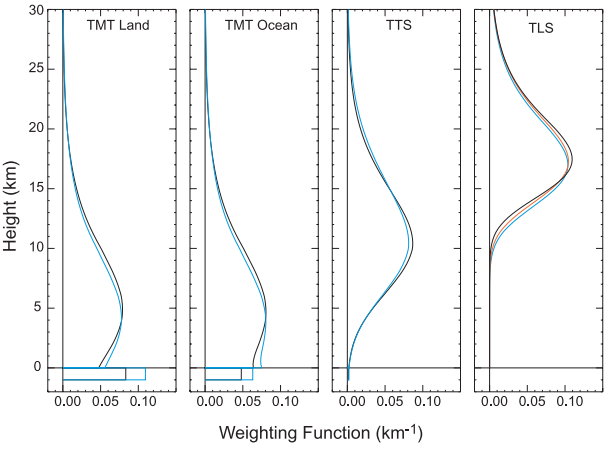

FIG. 2. Vertical weighting functions for each MSU and AMSU channel. The MSU weighting functions (which use the central five views) are shown in black; the corresponding AMSU weighting functions (using the central 12 views) are shown in blue. The boxes below zero height represent the surface weight. For TMT, land and ocean weighting functions are shown separately; for the other two channels, the land and ocean weighting functions are almost identical to each other. Note the lower peak and increased surface weight for AMSU TMT (channel 5) relative to MSU (channel 2). This leads to an increase in brightness temperature that must be removed empirically before merging data from the two different instruments. There is also a large difference between the weighting functions for AMSU TLS (channel 9) and MSU (channel 4). We use an off-nadir set of AMSU views, whose weighting function is shown in red, to help reduce the differences before merging.

atmosphere. The second term is due to radiation emitted in the downward direction propagating to the surface and then being reflected upward, with attenuation along both the downward and upward paths. Increasing the zenith angle, and thus the path length through the atmosphere, increases both the emission by each layer and the absorption terms. When combined, these effects cause the surface weight to be reduced and the peak of the temperature weighting function to move higher in the atmosphere.

Both MSU and AMSU make observations within a complex of oxygen emission lines near 60 GHz, whose width varies rapidly as a function of pressure, primarily because of collision-induced broadening. In the stratosphere, each line is clearly separated from its neighbors. As the pressure increases, the lines begin to broaden and merge together. By 300 hPa, the lines have merged into a single broad line, with the MSU and AMSU measurement frequencies on the lower shoulder (see Fig. 1). Because the line width in the stratosphere is significantly less than the measurement bandwidths, it is necessary to perform radiative transfer calculations at a number of frequencies within each measurement band and then average these results together to obtain an accurate weighting function for each MSU–AMSU channel. This is particularly true for MSU channels 3 and 4 and for the corresponding AMSU channels 7 and 9. Below, we discuss each pair of the three sets of corresponding MSU and AMSU channels separately.

1) MSU2 and AMSU5. AMSU Channel 5 (AMSU5) is a double sideband receiver sensitive to two sidebands at 53.71 and 53.48 GHz, each with a bandwidth of 170 MHz. MSU channel 2 (MSU2) is a single sideband receiver with sensitivity at 53.74 GHz with a bandwidth of 200 MHz (see Fig. 1). In the left two panels in Fig. 2, we plot vertical weighting functions for the mean of the central 5 views of MSU2, and the mean of the central 12 views of AMSU5 for simulated land and ocean views using the 1976 U.S. Standard Atmosphere. These calculations were made using a radiative transfer model based on Rosenkranz (1993; 1998) and our model of the ocean surface (Wentz and Meissner 2000). Land surface emissivity was assumed to be 0.9, independent of incidence angle, an approximation which is supported by measurements at 37 and 85 GHz (Prigent et al. 2000). The resulting weighting functions for AMSU5 peak about 500 m closer to the surface, and the contribution of the surface is increased by about 35% relative to the MSU2 weighting function. Taken together, these changes result in a brightness temperature increase for AMSU5 relative to MSU2 of between 1.0 K and 3.0 K, depending on the surface type and local atmospheric profile. These differences must be removed before the AMSU results can be

merged with the previous MSU data–see section 4e for a description of our method.

2) MSU3 and AMSU7. AMSU7 is sensitive to a single band centered to 54.94 GHz, with a bandwidth of 380.5 MHz, and MSU3 is sensitive to a single band centered at 54.96 GHz, with a bandwidth of 200 MHz. Because the center frequencies are so similar, the shape of the weighting function in the low to midtroposphere is very similar between the two channels. The greater width of the AMSU7 measurement band leads to significantly more weight in the lower stratosphere than for MSU3 when the central 5 (MSU) and central 12 (AMSU) views are used (see Fig. 2) because more of the wings of the individual lines are sampled at low pressure by the wider measurement band (see Fig. 1). This difference leads to a brightness temperature decrease for AMSU 7 relative to MSU 3 of several tenths of a degree (K). The difference is greatest in the tropics where the vertical lapse rate is the largest in the upper troposphere and lower stratosphere. These differences are also removed using a method similar to that used for MSU2/AMSU5.
3) MSU4 and AMSU9. AMSU9 is sensitive to a single band centered at 57.29 GHz, with a bandwidth of 310 MHz, whereas MSU4 is sensitive to a single band at 57.94 GHz, with a bandwidth of 200 MHz. It can be seen in Fig. 1 that the AMSU9 measurement band is located between a lower-frequency pair of absorption lines than MSU4 and thus shows a lower absorption coefficient at all pressures. This leads to a weighting function for AMSU9 that peaks about 500 m lower in the atmosphere than the weighting function for MSU4. Because the mean lapse rate is relatively small in the region where the difference between the weighting functions is largest, the average temperature difference is only a few tenths of a degree (K). However, the difference in weighting functions leads to large differences in both the seasonal cycle and the response to stratospheric warming events in the polar regions. Unlike the case for the lower-frequency channels, these differences are not well accounted for by a simple location- and time-of-year-dependent difference because of both the nonperiodic nature of the stratospheric warmings and the greater difference between the weighting functions. Instead, before removing the residual differences empirically, we choose to better match the intra-annual behavior of the two channels by using a set of AMSU views with larger incidence angles, and thus longer slant paths through the atmosphere, which moves the peak of the weighting function farther above the surface.

TABLE 1. MSU and AMSU channels.

MSU channel	AMSU channel	Combined channel	Acronym
2	5	Temperature middle troposphere	TMT
3	7	Temperature troposphere–stratosphere	TTS
4	9	Temperature lower stratosphere	TLS

In Table 1, we list the MSU and AMSU channels that are combined to form our new datasets, as well as the names given to the resulting channels, following Christy et al. (2000). These names will be used in the remainder of this paper. It is important to note that although the MSU2/AMSU5 combination is called middle troposphere temperature (TMT), this channel also has significant (5%–15%) weight in the stratosphere, so that any tropospheric warming may be partly masked by the contribution of stratospheric cooling. By studying a weighted combination of TMT and lower stratosphere temperature (TLS) measurements, Fu et al. (2004) estimate that this effect cools global TMT trends by ~0.04 K decade^{-1} over 1979–2005.

c. *Instruments studied*

In this work, we have investigated use of the data from the nine MSU instruments, and the AMSU instruments on *NOAA-15* and *NOAA-16*. The premature malfunction of the AMSU instrument on the *NOAA-17* platform yields a dataset too short in duration to contribute significantly to a long-term time series. Because four instruments (MSU on *NOAA-14* and the three AMSUs) to operate after its failure, its use would bring little new long-term information to the data product. Currently there is less than 2 yr of data available from the *NOAA-18* instrument, so these data have been omitted from our analysis. We have also not yet attempted to include data from the AMSU instruments on *Aqua* or *MetOp-A*. In the next section, we describe the drifts observed between the AMSU instruments on *NOAA-15* and *NOAA-16* and our decision to exclude *NOAA-16* data from our combined dataset.

3. Spurious drifts in measurements from *NOAA-16*

We find significant differences in interannual trends between *NOAA-15* and *NOAA-16* that we conclude are due to drifts in the *NOAA-16* instrument. An important part of our evidence that supports this conclusion is based on the inconsistency of the *NOAA-16* data between

channels and view angles, including measurements from other nearby AMSU channels that are not used in our final data products. These channels are AMSU4 (peaks at the surface), AMSU6 (peaks at ~8 km, ~350 hPa), and AMSU8 (peaks at ~13 km, ~165 hPa). We focus on data over the tropical oceans (30°S to 30°N) because a number of calibration issues are simpler in this region. First, the average annual cycle is relatively small in the tropics, reducing the tendency for differences in sampling during a month to add error to the monthly average. Second, the diurnal cycle for those channels (AMSU4 and AMSU5) that sense a significant amount of signal emitted by the surface is much reduced for ocean scenes (Mears et al. 2003). We formed monthly time series of brightness temperature for each instrument, channel, and field of view for the time period (2001–06) when both instruments were operating simultaneously. The time series were investigated for evidence of both overall drifts of one instrument relative to the other, and also for evidence of ''target factor''-type calibration issues, which result when a calibration error proportional to the temperature of the calibration target is present in one or more instruments (Christy et al. 2000). Over this time period, all channels investigated, except for channel 4 (and to a lesser extent) channel 9, showed large trend differences between *NOAA-15* and *NOAA-16* data.

The challenge presented by these apparent drifts is that we have no absolute temperature references in the upper air that would make it possible for us to unambiguously decide which instrument is producing data that is closer to the truth. We have concluded that radiosonde datasets are not suitable for this task, given the possibility of large errors at high altitude (Lanzante et al. 2003; Randel and Wu, 2006; Sherwood et al. 2005), and datasets based on GPS measurements (e.g., Ho et al. 2007) do not have a sufficient number of samples early in the overlap period. We instead check the internal consistency of the data from each AMSU instrument, similar to the method used by Fu and Johanson (2005) to evaluate different MSU datasets. The measurements, and in particular interannual-scale changes, should be consistent both between nearby channels and between nadir and limb measurements for the same channel. In Fig. 3, we show a bar graph of the trends over this time period for the nadir (an average of the central 12 fields of view, views 10–21) and the limb (an average of the outer eight fields of view, views 1–4 and 27–30) for each satellite. (Because of longer slant paths through the atmosphere, the vertical weighting function for limb views is typically centered a kilometer or two higher in the atmosphere than the corresponding nadir views.)

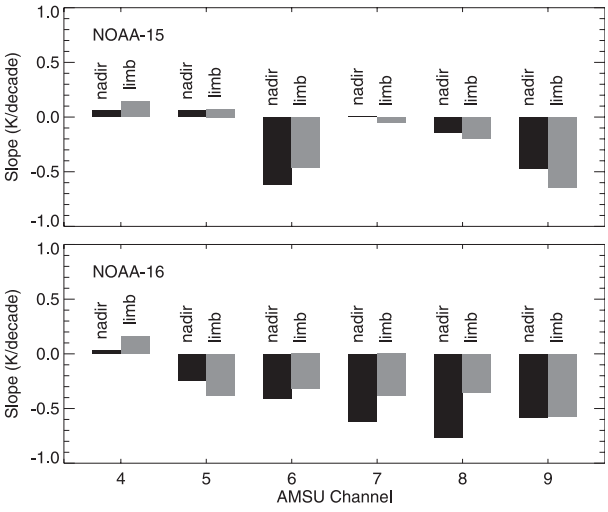

FIG. 3. Tropical (30°S to 30°N) oceanic temperature trends over the time period 2001–06 for the *NOAA-15* and *NOAA-16* AMSU instruments. Trends are computed separately for near-nadir and near-limb sets of views. The more consistent data from *NOAA-15* (except for channel 6) lead us to conclude that *NOAA-16* is very likely to be suffering from significant calibration drifts.

By evaluating the data both as presented in this plot and in a number of other ways, including difference time series between instruments for each channel and field of view, and trends as a function of the field of view for each instrument, we have come to the following conclusions.

First, channel 6 appears to be drifting in both satellites. Its large negative trend is inconsistent with channels 5 and 7 for *NOAA-15* (and with MSU2 and MSU3 data from *NOAA-14*, not shown). Second, if channel 6 is excluded, the rest of the channels from *NOAA-15* form a consistent set of observations, with trends that increase slightly as we leave the surface and then decrease as more stratospheric cooling signal is included. Note that for channels 7 though 9 the limb views show a more negative trend than the nadir view, as expected, because the limb views have weighting functions that peak higher in the stratosphere. The behavior of the limb–nadir views is more complicated for channels 4 and 5 because of the competing effects of changes in trend with height in the troposphere (the trends are expected to increase with height over much of the globe), increased contribution from the stratosphere, and changing oceanic surface emissivity with angle and polarization.

Third, data from *NOAA-16* are not internally consistent, even if we ignore channel 6. Trends for the limb views are typically less negative (by a large amount) than the nadir views for channels 6 through 9. It would be impossible to construct a vertical trend structure consistent with *NOAA-16* measurements that did not show

unreasonably large changes in trend with small changes in altitude. Also, data from channel 5 are inconsistent with *NOAA-15* and MSU2 data from *NOAA-14*, and data from channel 7 are inconsistent with *NOAA-15* and MSU3 data from *NOAA-14*. Data from channel 4 are consistent with measurements from *NOAA-14* and *NOAA-15*; thus, channel 4 may be free from drifts.

Based on these arguments, we have decided to not use *NOAA-16* data to construct a merged dataset. We are continuing to study this problem, and it is possible that we will be able to adjust for these drifts in the future if we develop sufficient understanding of the cause of these drifts. In the future, measurements from the AMSU instruments on the *NOAA-18*, *MetOp-A*, and *Aqua* satellites, as well as data from the conically scanning Special Sensor Microwave Imager/Sounder (SSMIS) may prove useful for further evaluation of this problem.

4. Detailed description of the merging procedure

a. Premerge adjustments

Before merging, each MSU and AMSU observation is subjected to a number of processing, quality control, and adjustment steps. These steps are discussed in detail for the case of MSU channel 2 in a previous paper (Mears et al. 2003). For the additional MSU channels, as well as for AMSU, many of these steps are the same as those for MSU2; thus, we only discuss the most important steps here.

For the near-nadir view subsets (MSU2_N5 and AMSU5_N12), each observation is adjusted to correspond to the nadir view so that the difference between measurements at different incidence angles is diminished, thereby reducing sampling noise in the final product.[1] This adjustment also removes the small effects of changes in the incidence angle due to variations in both the earth's radius of curvature and in orbital height, and thus the effects of orbital decay. The adjustment is made using simulated brightness temperatures calculated from a National Centers for Environmental Prediction (NCEP) reanalysis–based atmospheric profile climatology (Kalnay et al. 1996; Mears et al. 2003). We found that the global average of the difference between the modeled and measured temperatures was still not zero or symmetric about the nadir. For MSU, we found that we had to include an additional term that was well modeled as an instrument roll (Mears et al. 2003). For the AMSU on *NOAA-15*, we found that after performing the model-based nadir adjustment, an additional empirical correction $T_0(\text{fov})$ for each field of view (not well described by an instrument roll) was needed to force the adjusted globally averaged brightness temperatures to be an independent of field of view:

$$T_{\text{Adj}}(\text{nadir}) = T_{\text{AMSU}}(\text{fov}) + T_{\text{Mod}}(\text{nadir}) - T_{\text{Mod}}(\text{fov}) + T_0(\text{fov}), \quad (5)$$

where T_{Adj} is the adjusted temperature, T_{AMSU} is the measured temperature, and T_{Mod} is the simulated brightness temperature from the NCEP-based climatology, interpolated in location at a time of year to match the observation undergoing adjustment. The empirical corrections $T_0(\text{fov})$ are typically a few tenths of a Kelvin and are independent of location on the earth and time of year; they thus have a negligible effect on long-term behavior. These are largest near the two ends of the scan and are likely to be due to spillover effects.

A second important correction accounts for drifts in local measurement time, which can alias any diurnal cycle into the long-term time series if it is not corrected. Using 5 yr of hourly output from the NCAR Community Climate Model (CCM3) climate model (Kiehl et al. 1996), we created a diurnal climatology for MSU channels 2–4 and AMSU channels 5, 7, and 9 as a function of earth location, time of day, time of year, and incidence angle using the methods described in Mears et al. (2002). This diurnal climatology was then used to adjust each measurement so that it corresponds to local noon. The adjustments are largest for MSU2 and AMSU5 because of the contribution of surface emission to these channels. Surface emission can have a large diurnal signal, particularly in arid land regions. These regions dominate the global average of the MSU2 and AMSU5 adjustments. In Fig. 4, we show time series of the global (−82.5 to 82.5) mean of the adjustments applied to each MSU and AMSU channel for the *NOAA-14* (MSU) and *NOAA-15* (AMSU) satellites. Because the characteristics of the diurnal cycle vary with time of year and location, there are significant annual and semiannual signals in the adjustment for each channel. The diurnal adjustment for AMSU5 is about 40% larger than that for MSU2 for the same crossing time. This is because 1) the surface contribution for AMSU5 is about 35% larger than MSU2 and 2) the AMSU5 weighting function has more weight near the bottom of the troposphere, where

[1] For AMSU9, which uses a combination of eight limb views, the adjustment to nadir is not performed because it would result in lowering the effective weighting function of the view combination. For this channel, we use a simple average of the eight limb views that have been adjusted to a constant view angle for each view, and with empirical field-of-view corrections removed.

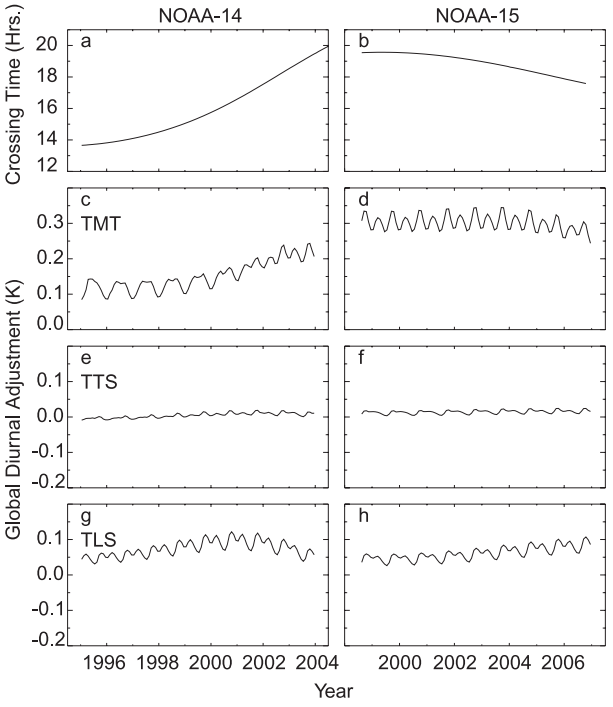

FIG. 4. Examples of the adjustments applied to the individual satellite data to account for changing measurement time. (a),(b) The ascending node equator crossing time for the (a) *NOAA-14* and (b) *NOAA-15* satellites; (c)–(h) the global average of the adjustments applied to (c) MSU2, (d) AMSU5, (e) MSU3, (f) AMSU7, (g) MSU4, and (h) AMSU9. The adjustments for *NOAA-14* are larger because the measurement time of the *NOAA-14* platform changed more over the 9-yr period.

the diurnal cycle is large over land areas. It is possible that significant errors are present in the CCM3-derived diurnal cycles, since errors have been demonstrated to be present in the diurnal cycle of cloud cover and precipitation, and the diurnal cycle in near-surface air temperature appears to be too small in the model (Dai and Trenberth 2004).

b. Choice of views used for each channel

The first step in our merging procedure is to choose a set of AMSU views to be combined to match the MSU data. In making this choice, we balanced the competing factors of closely matching the brightness temperatures, similar spatial and temporal sampling, and simplicity. For all three of the MSU–AMSU products described here, the central five fields of view for MSU are used. As noted in section 2b above, there are differences between the vertical weighting functions of the MSU measurements and the corresponding AMSU measurements because of differences in measurement frequency and bandwidth. In principle, we could use a weighted average of AMSU measurements with different incidence angles and different measurement frequencies (i.e., other AMSU channels) to produce a synthetic measurement that closely matches the MSU channel of interest. In practice, this results in very different spatial sampling than the original MSU measurements. This method can also lead to increased noise. This is especially true if there are large differences in the weights used, if some weights are negative, or if views are included that are too far from the nadir. If measurements from other AMSU channels are used, additional complications due to potential calibration errors in those channels are also possible. In section 3, we found that the *NOAA-15* AMSU6 channel has significant calibration problems, eliminating it from consideration. Our approach is to use a simple combination of AMSU views unless we find it to be necessary to use a more complicated approach.

For MSU2–AMSU5 and MSU3–AMSU7, we found that we can use the central 12 AMSU views (i.e., those nearest the nadir). This results in a swath width very close to the swath defined by the central five views of the MSU instrument because of the smaller footprint and smaller angular spacing between adjacent views for AMSU compared to MSU.

For MSU4–AMSU9, we choose to use a set of 8 AMSU views (views 7–10 and 21–24) that span a range of earth incidence angles from 24.5° to 36.3°. The difference between the MSU4 and AMSU9 measurement frequencies is large enough that significant errors arise if the near-nadir AMSU views are used. The set of eight off-nadir views represents a compromise between the best match of the vertical weighting function to the MSU4 weighting function and avoidance of near-limb views, where the incidence angle changes rapidly with view number, thereby increasing noise in the averaged product. The vertical weighting function for this set of views, shown in red in Fig. 2d, is significantly closer to the MSU4 weighting function than the near-nadir view set. Because the weighting function match is far from perfect, we expect that there will be significant differences between the MSU4 and AMSU9 data, which will be removed later in the merging process.

By averaging over these view combinations, we compute monthly mean gridded (2.5° × 2.5°) antenna temperatures for each satellite, with the measurement time and view angle corrections included. We also compute monthly averaged temperatures for the calibration targets on the same grid. These monthly averages are used for all the subsequent steps in the merging procedure. This is different from our earlier methods, which used a combination of 5-day zonal averages and daily gridded averages to merge the gridded data (Mears et al. 2003;

Mears and Wentz 2005). The new method is computationally more efficient and results in insignificant changes in the merged dataset.

c. Error model

Global averages of simultaneous measurements made by co-orbiting MSU instruments differ by both a time-invariant intersatellite offset and an additional term that is strongly correlated with the variations in temperature of the hot calibration target for each satellite. This effect was first noticed by Christy et al. (2003). The exact physical cause of this small calibration error is not known. Possible causes include residual nonlinearity in the radiometer response that was not adequately measured during ground calibration or an error in the specification of the effective brightness temperature of the calibration target. This second error could be due to a combination of any of the following effects: 1) temperature gradients between the precision thermistors and the emitting surface, 2) errors in the calibrations of these thermistors, 3) a nonunit emissivity of the calibration target, or 4) antenna spillover around the target causing other sources (either warm satellite parts or cold space) to be sensed during the calibration procedure. It is also possible that the source of error is due to changes in the temperature of the radiometer electronics that result in a change in receiver parameters. To first order, such changes are removed by the two-point calibration procedure, but changes in absolute noise levels, coupled with nonlinearity in the receiver, could also result in the observed behavior. These various causes are difficult to separate using on-orbit analysis techniques because they lead to similar behavior as a function of calibration target temperature (or instrument temperature, which closely tracks calibration target temperature) and scene temperature. The source of error may be a combination of several of these factors, including nonlinearity, temperature specification, and instrument temperature effects. An additional complication is that any nonlinearity in radiometer response may be dominated by cubic or other higher-order terms because the NOAA nonlinearity correction procedure implemented in routine processing minimizes quadratic nonlinearity by design.

All the types of errors discussed above also cause an error that depends on the brightness temperature being sensed or the scene temperature (Grody et al. 2004). Because the globally averaged seasonal cycle for each channel is relatively small, scene temperature–related effects are small and difficult to separate from the much larger target temperature effects when global averages are considered. Our earlier work focused on global averages, and thus we omitted scene temperature effects. Scene temperature–dependent errors may be an important contributor to latitude dependence of intersatellite offsets and are important in polar regions where the seasonal cycle in atmospheric temperature is very large.

Instead of attempting to determine the physical source of the calibration errors unambiguously, we use an empirical error model for brightness temperature incorporating the target temperature and scene temperature correlation:

$$T_{\mathrm{MEAS},i} = T_0 + A_i + \alpha_i T_{\mathrm{TARGET},i} + \beta_i T_{\mathrm{SCENE}} + \varepsilon_i, \quad (6)$$

where T_0 is the true brightness temperature, A_i is the temperature offset for the ith instrument, and α_i is a small multiplicative target factor describing the correlation of the measured antenna temperature with the temperature anomalies of the hot calibration target, $T_{\mathrm{TARGET},i}$. The parameter β_i describes the correlation of the calibration error with the scene temperature anomaly T_{SCENE}, and ε_i is an error term that contains additional uncorrelated, zero-mean errors due to instrumental noise and sampling effects. This model is an extension of the model used by both Christy et al. (2003) and Mears et al. (2003) in that it now includes the scene temperature dependence. We find the scene temperature term necessary to reduce seasonally dependent intersatellite differences in the polar regions. The new model is also closely related to the physically based error model proposed by Grody et al. (2004). We describe this relationship in the appendix.

A central question is whether the merging parameters (A_i, α_i, and β_i) should be constant for each satellite or be allowed to vary with earth location (e.g., latitude). Further analysis of our earlier results from Mears et al. (2003), where the values of A_i and α_i are constants for each satellite, revealed residual latitude-dependent intersatellite differences after global-mean offsets were removed, which we plot as gray lines in Fig. 5. Our goal is to reduce these differences while introducing as few new merging parameters as possible. These residual offsets appear to be related to scene temperature, being either negative in the tropics and positive near the poles or vice versa. We hoped that by adding the T_{SCENE} dependence via spatially constant β parameters, we would be able to satisfactorily reduce the latitude-dependent offsets. Although this reduced the residual offsets significantly (see blue lines in Fig. 5), we concluded that the offsets were not yet small enough to have a negligible effect on the long-term behavior of the merged product. This led us to allow the intersatellite offsets A_i to vary with latitude, while keeping the target factors α_i constant. This reduced the average offsets nearly to zero (black lines in Fig. 5), leaving only small seasonally dependent intersatellite differences near the poles, which we then reduce using

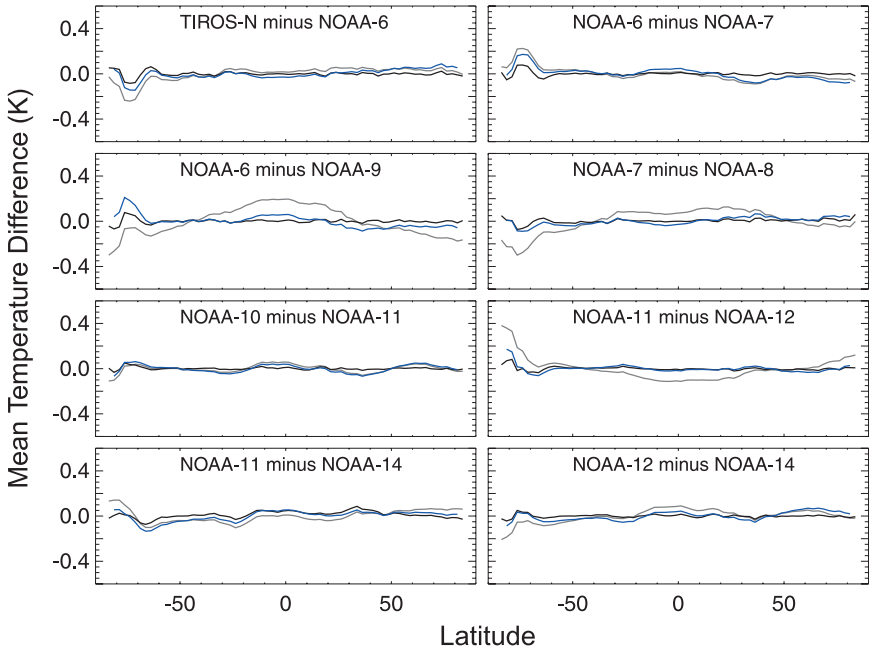

FIG. 5. Intersatellite differences as a function of latitude for several MSU2 satellite pairs. The gray lines are the differences that occur when the offsets applied to each satellite are constants independent of latitude. The blue lines are the differences that occur when a scene temperature–dependent offset is used. The black lines are the differences after empirically determined latitude-dependent offsets are applied. The black lines are different from zero because of the north–south smoothing applied to the offsets and because most satellites have overlaps with two or more other satellites. The regressed offsets minimize all intersatellite differences, which often results in nonzero differences for a given satellite pair. For several satellite pairs, the black lines are significantly closer to zero than the blue lines, indicating that the empirical method does a better job of removing the latitude dependence of the offsets than the scene temperature–dependent model. Other MSU channels show results that are different in detail but have similar or larger variability as a function of latitude.

the scene temperature dependence, with a single β_i for each satellite calculated, independent of latitude. In the next four sections, we describe the merging procedure in more detail.

d. Determining the values for the target factors

We determine the target factors using an analysis of observations of observations averaged over the latitude range 50°S to 50°N. We exclude the polar regions to reduce the effects of the seasonal cycle via the scene temperature dependence on the derived values of α_i. We perform calculations separately for the MSU and AMSU sets of satellites. This is because there are differences between the MSU and AMSU data that are often dominated by a seasonal-scale signal caused by small differences in the vertical weighting functions combined with seasonal changes in the vertical temperature profile and/or surface emission. The target temperature time series also often contains large seasonal components. If both MSU and AMSU data were included in the same regression, the resulting target factors would be influenced by this seasonal signal in the MSU/ASMU differences that does not arise from effects related to the temperature of the calibration target and would result in erroneous values for the target factors.

For each month when two or more satellites are observing simultaneously, we form an equation by taking the difference between versions of Eq. (6) for each satellite pair,

TABLE 2. Target factors.

	MSU2	MSU3	MSU4
TIROS-N	0.0024	N/A	0.0032
NOAA-06	0.0019	N/A	0.0171
NOAA-07	0.0084	N/A	0.0148
NOAA-08	0.0329	N/A	0.0269
NOAA-09	0.0362	N/A	−0.0087
NOAA-10	0.0049	−0.0138	0.0079
NOAA-11	0.0300	0.0231	−0.0159
NOAA-12	0.0079	0.0214	0.0170
NOAA-14	0.0249	0.0241	0.0115
NOAA-15	0.0002	−0.0027	−0.0048

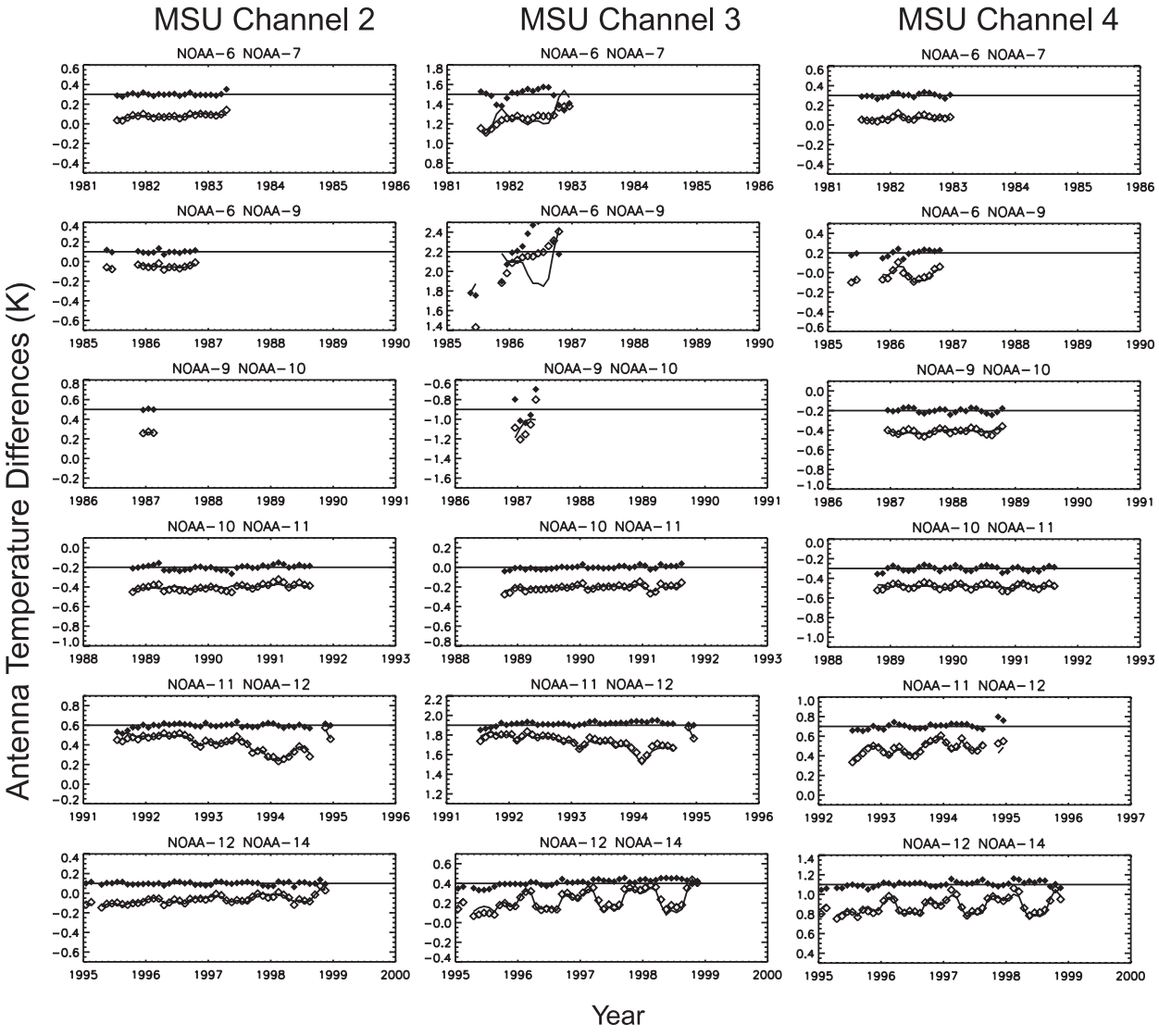

FIG. 6. Time series plots of the global mean (50°S–50°N) differences between some representative satellite pairs. The open symbols are the differences before the target temperature adjustment is applied, and the curved line is the best fit to these differences using the target temperatures for each satellite as the independent variables. The solid symbols are the residuals after the fit, offset so that the zero value is the horizontal line. Satisfactory fits are obtained for all overlaps except for the MSU channel 3 differences that involve *NOAA-6* or *NOAA-9*, indicating that these satellites exhibit drifts that are not well explained by the target temperature effect.

$$T_{\mathrm{MEAS},i} - T_{\mathrm{MEAS},j} = A_i - A_j + \alpha_i T_{\mathrm{TARGET},i} - \alpha_j T_{\mathrm{TARGET},j}, \quad (7)$$

thus eliminating the true brightness temperature. For now, we ignore the scene temperature term (which will be discussed in section 4f). For MSU, this results in a system of equations with 190 equations in 17 unknowns (eight offsets and nine target factors; note that one offset, $A_{\mathrm{NOAA\text{-}10}}$, is arbitrarily set to zero to prevent a singular system of equations). The system is then solved using singular value decomposition to find the target factors. The offset values are discarded. The final values for the offsets will be determined as a function of latitude in the next step. The values of the target factors determined for each MSU channel are tabulated in Table 2. For MSU2 and MSU4, this procedure results in an acceptable solution for all nine MSU satellites. For MSU3, we find that there are large drifts in the measurements made by *NOAA-6* and *NOAA-9* that are not explained by our error model, as we show in Fig. 6. For MSU3, we only use satellites from *NOAA-10* onward; thus, the MSU3 dataset begins in December 1986 instead of November 1978.

The *NOAA-15* target factor is more difficult to define. As discussed above, seasonal scale differences between MSU and AMSU preclude use of MSU/AMSU differences. The drift of *NOAA-16* relative to *NOAA-15* complicates the use of *NOAA-15–NOAA-16* differences because we do not want the drift to affect the target factor for *NOAA-15*. To prevent this, we use a method analogous to that used for MSU except that we remove a linear trend from both the intersatellite differences and the target factors before we perform the regression. This results in target factors that remove seasonal-scale fluctuations but are not affected by long-term trends. The validity of this approach depends on the assumption that whatever is causing *NOAA-16* to drift does not cause spurious seasonal-scale fluctuations. The *NOAA-15* target factors are also shown in Table 2.

e. Latitude-dependent offsets

The next step is to determine the latitude-dependent offsets. To do this, we average the gridded data over longitude to produce averages over each 2.5° zonal band. For each zonal band, we solve a system of equations given by

$$T_{\mathrm{MEAS},i,k} - T_{\mathrm{MEAS},j,k} = A_{i,k} - A_{j,k} + \alpha_i T_{\mathrm{TARGET},i,k} - \alpha_j T_{\mathrm{TARGET},j,k}, \quad (8)$$

which is a version of Eq. (7) generalized so that each equation describes the difference between measurements made by the *i*th and *j*th satellites for the *kth zonal band*, where the values of $A_{i,k}$ are allowed to vary with latitude. The target factors α_i are fixed to the values in Table 1 and the equations are solved for each zonal band. To prevent a singular set of equations, we must set the overall offset to a fixed value. We choose to set the offset for *NOAA-10* to zero for all latitudes. This assumption affects the absolute values of the measurements made but has no effect on the long-term changes that are the focus of this study. The offset values for each satellite are then smoothed in the north–south direction using a mean-of-seven ''boxcar'' smoother. The differences between the MSU instruments and the AMSU instrument on *NOAA-15* are too complex to be adequately described by latitude-dependent constant offsets and are addressed in section 4h.

f. Scene temperature–dependent errors

When we apply the target factors and offset determined in the previous steps to the data and evaluate the intersatellite differences, we find that there are significant seasonal-scale fluctuations near the poles, where the seasonal cycle is large, but not near the equator, where the seasonal scale is small. This suggests that part

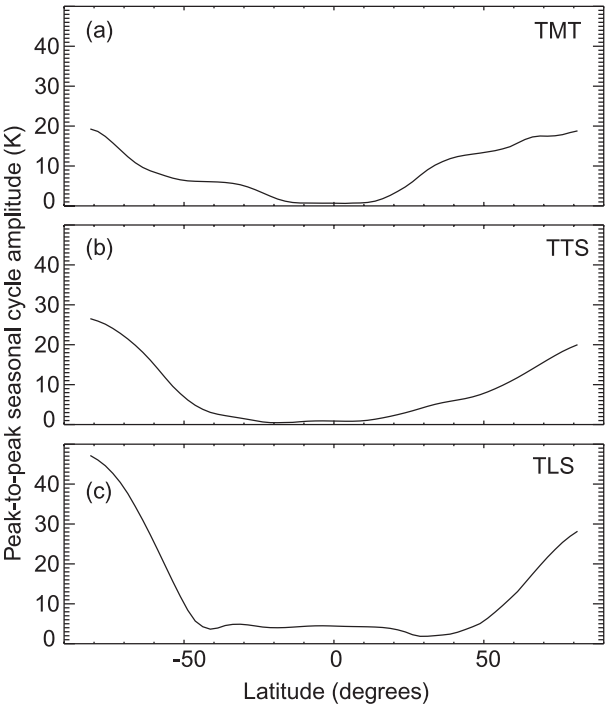

FIG. 7. Peak-to-peak amplitude of the seasonal cycle as a function of latitude for each of the three channels. The seasonal cycles are calculated using the MSU-measured mean monthly antenna temperatures over the 1979–98 period. The seasonal-scale variability these plots describe is multiplied by the scene temperature factors in Table 3 to produce the scene temperature adjustments: (a) TMT, (b) TTS, and (c) TLS.

of the remaining differences is caused by a scene temperature–related calibration error. To remove this, we again take the difference between versions of Eq. (7) for each month that two or more satellites are observing simultaneously. Substituting the values already determined for $A_{i,j}$ and α_i into

$$T_{\mathrm{Adj},i,k} = T_{\mathrm{MEAS},i} - A_{i,k} - \alpha_i T_{\mathrm{TARGET},i,k}, \quad (9)$$

and keeping the T_{SCENE} dependence from Eq. (6), we obtain a system of equations given by

TABLE 3. Scene temperature factors.

	MSU2	MSU3	MSU4
TIROS-N	0.0084	N/A	0.0037
NOAA-06	0.0124	N/A	0.0001
NOAA-07	0.0087	N/A	−0.0076
NOAA-08	0.0024	N/A	0.0026
NOAA-09	−0.0056	N/A	0.0025
NOAA-10	−0.0054	0.0151	0.0108
NOAA-11	−0.0110	0.0092	0.0093
NOAA-12	−0.0028	−0.0062	−0.0082
NOAA-14	−0.0070	−0.0181	−0.0056
NOAA-15	0.0000	0.0000	0.0000

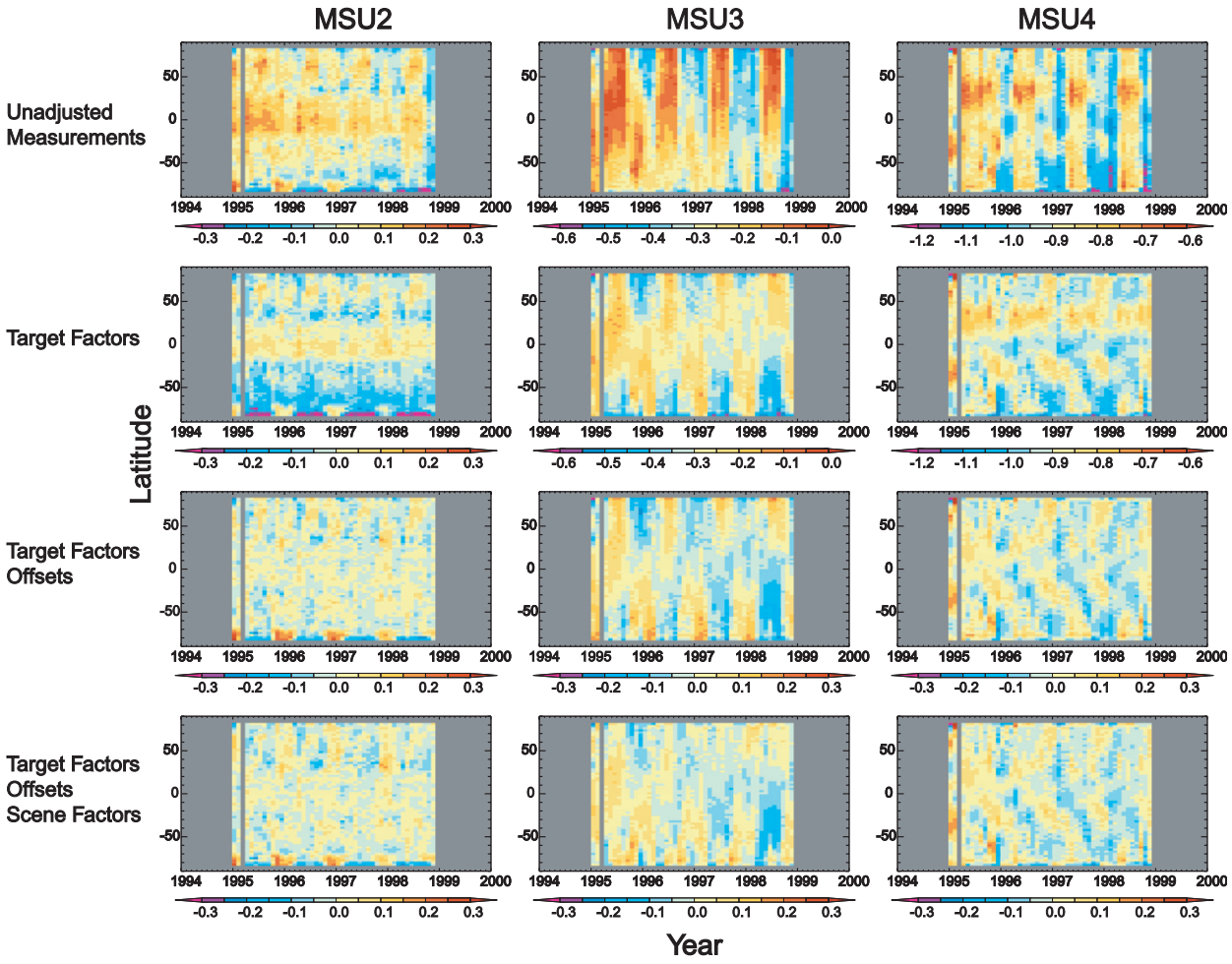

FIG. 8. Time–latitude plots of the MSU intersatellite differences (*NOAA-12* minus *NOAA-14*) for each of the three channels studied at different stages in the intercalibration process. (top) Uncalibrated data with only the diurnal and incidence angle adjustments made. Note the drifts and seasonal-scale oscillations in the time direction in each channel. (second row) Differences after the target temperature adjustments are applied. The large drift apparent in MSU2 has been removed, as well as much of the periodic differences in MSU3 and MSU4. In MSU2 there remains a latitude-dependent offset. (third row) Differences after the latitude-dependent offsets are applied. Most differences are now less than 0.05 K, except for a significant seasonal oscillation in the southern polar region in MSU2 and MSU3, which is reduced somewhat by (bottom row) the scene temperature adjustments.

$$T_{\mathrm{Adj},i,k} - T_{\mathrm{ADJ},j,k} = \beta_i T_{\mathrm{SCENE},i,k} - \beta_j T_{\mathrm{SCENE},j,k} = (\beta_i - \beta_j) T_{\mathrm{SCENE},k} \quad (10)$$

for each zonal band. We can replace $T_{\mathrm{SCENE},i,k}$ and $T_{\mathrm{SCENE},j,k}$ with $T_{\mathrm{SCENE},k}$ because the scene temperature is independent of the satellite index; T_{SCENE} is closely approximated by the measured antenna temperatures. To prevent noise in the measurements from unduly influencing the derived values for β, we use for T_{SCENE} an average scene temperature. This average is found by averaging the results from all satellites over the 1979–98 period together to form an antenna temperature climatology that depends on latitude and month. These values are then used in the system of equations described by Eq. (8) to deduce the values of β. Because the β_i only appear in the equations as differences between values of β for different satellites, their average value is arbitrary. We use singular value decomposition to choose the minimal-variance solution for the β_i because we want to change the data by the smallest possible amount. We report the values for β for each channel and satellite in Table 2 and in Fig. 7. We plot the amplitude of the seasonal cycle as a function of latitude for each satellite.

To summarize the effects of these various intercalibration steps, we show in Fig. 8 color-coded time–latitude plots of the intersatellite differences at different stages in the intercalibration process for each channel for an example pair of satellites, *NOAA-12* and *NOAA-14*.

TABLE 4. Average intersatellite difference statistics.

	TMT		TTS		TLS	
	RMS	σ	RMS	σ	RMS	σ
Raw	0.225	0.046	0.854	0.082	0.537	0.049
Target factors	0.217	0.016	0.866	0.024	0.537	0.021
Target factors, offsets	0.017	0.016	0.025	0.025	0.023	0.021
Target factors, offsets T_b factors	0.017	0.016	0.025	0.025	0.023	0.021

The amount and spatial–temporal structure of reduction of intersatellite differences between other pairs of satellites after each intercalibration step is similar. In Table 4 we show mean intersatellite difference statistics for each step. The RMS and standard deviation of global monthly differences for each pair of overlapping satellites are averaged together, weighted by the number of months in each overlap. Applying the target factors reduces the standard deviation considerably, with little effect on the RMS differences, which are dominated by intersatellite offsets. When these are removed, the RMS differences decrease markedly. Applying the scene temperature factors has little effect on the global statistics but can improve the statistics near the poles substantially. For example, the standard deviation statistic for the latitude band from 82.5°S to 70°S is 0.101 K without the scene temperature correction and is reduced to 0.085 K with the correction.

g. Merging data from different satellites

After all the adjustments are applied to the MSU data, we evaluate the intersatellite differences for any remaining problems. We found that several satellites had averages for several months that appeared to be anomalously high or low. These typically occurred near the beginning or end of each satellite's lifetime. Often, these were associated with months for which several days of data were missing, causing sampling errors, or with times when data quality was noted to have deteriorated by the satellite operations team at NOAA (Goodrum et al. 2000; Kidwell 1998). In other cases, no cause could be identified. These spurious months, which are listed in Table 5, were removed from the data. The data from different satellites were then combined using simple averaging when data from more than one satellite was present. For AMSU, only one satellite is currently used; thus, no merging is necessary to produce an AMSU-only dataset. We anticipate future updates in which more AMSU satellites will be used. Methods similar to those used for MSU will be used to merge the AMSU data for those updates. A record of which satellites are used for each month is kept and propagated through subsequent steps to become part of the final data product.

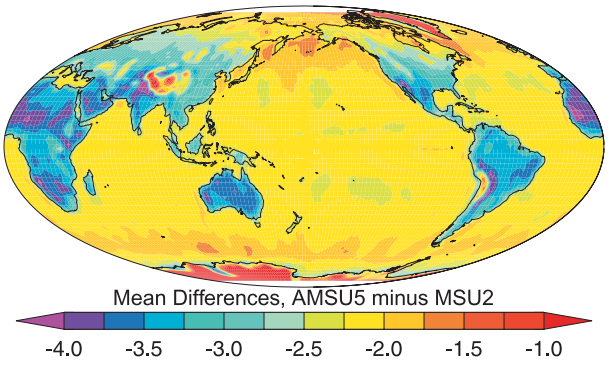

FIG. 9. Global map of the mean difference of antenna temperature between AMSU channel 5 and MSU channel 2 for the month of July, averaged over 1999–2004. The mean differences for each month are removed from the AMSU data before merging with MSU data.

h. Merging MSU and AMSU data

Because of the difference between the MSU and AMSU weighting functions for corresponding channels, there are small differences between the measured antenna temperatures that depend on the local atmospheric profile and surface temperature. We remove these differences on average by calculating the mean difference between MSU and AMSU measurements as a function of earth location and time of year. We then subtract the difference from the adjusted gridded monthly AMSU averages so that they match the corresponding MSU-only data. An example of these differences for MSU2–AMSU5 shown in Fig. 9. For MSU2–AMSU5, the spatial pattern in the difference is dominated by differences in surface type (i.e., land versus ocean). For MSU3/AMSU7 and MSU4–AMSU9, the spatial pattern in the differences showed the largest

TABLE 5. Satellite/months manually excluded from processing.

Satellite	TMT	TTS	Month excluded TLS
TIROS-N	March 1980	March 1980	March 1980
NOAA-06	April 1983	April 1983	April 1983
NOAA-11	October 1994–December 1994	N/A	September 1994–December 1994
NOAA-12	May 1991–September 1991	N/A	May 1991–December 1991

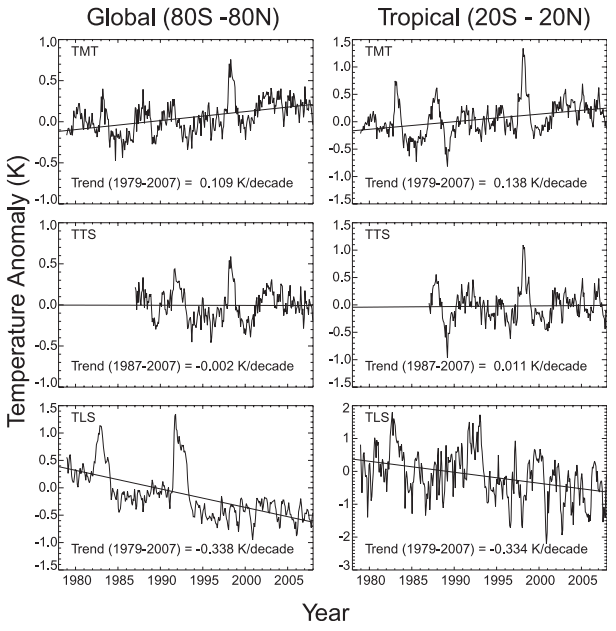

FIG. 10. (left) Global (80°S to 80°N) and (right) tropical (20°S to 20°N) temperature anomaly time series for each channel calculated from the merged data. Anomalies were calculated using a 1979–99 reference period, except for TTS values, which were calculated using a 1987–99 reference period. Also plotted are least squares linear fits (solid line) to the data over the periods shown in each plot.

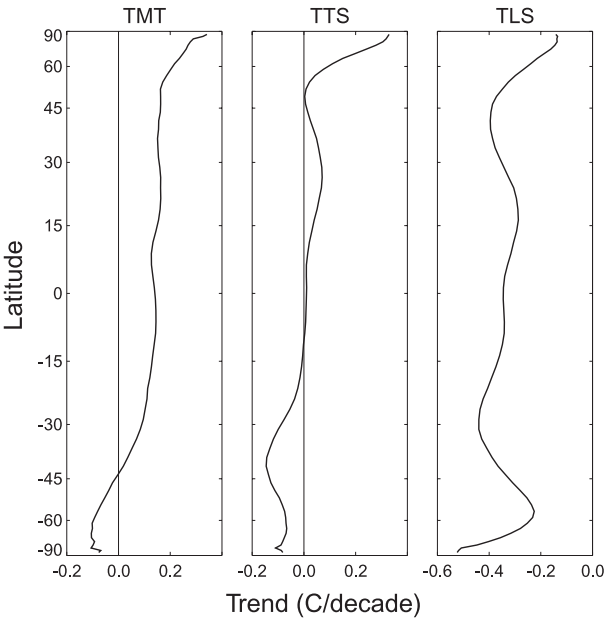

FIG. 11. Plots of the least squares linear trends calculated as a function of latitude for each channel. The time period of the fit is 1979–2007 for TMT and TLS and 1987–2007 for TTS.

variability in the midlatitudes, where sampling error is important. We choose to reduce the effect of sampling error for channels MSU3–AMSU7 and MSU4/AMSU9 by smoothing the difference maps by fitting to spherical harmonics $Y_{L,M}$ using values of L up to 9 and M between $-L$ and L. After the spatial/temporal adjustments are applied to the AMSU data, results from the two different instrument types are then merged, using simple averaging when data from both MSU and AMSU are present.

5. Results

The steps above result in a monthly gridded atmospheric temperature dataset for each channel. We have made data freely available online in a variety of formats. In the section below we briefly summarize the results by evaluating representative time series and decadal trends.

a. Global and tropical time series

In Fig. 10, we show global and tropical (20°S to 20°N) time series for each channel. The short-term behavior TMT is strongly influenced by warming associated with the ENSO events that occur in 1982–83, 1987–88, and 1997–98, especially in the tropics. Also present, but less obvious, are short-term cooling events associated with the increase in aerosols following the eruptions of El Chichon (1982) and Mt. Pinatubo (1991). Stratospheric warming events from these eruptions dominate the TLS time series. The TTS time series, which has weight approximately evenly divided between the troposphere and the stratosphere, shows a combination of both effects. The linear trends are least squares fits to the data. The trends are statistically significant at the 2σ level for TMT and TLS when evaluated using autocorrelation-adjusted goodness-of-fit criteria (Seidel et al. 2004).

b. Latitude dependence of trends

In Fig. 11, we plot the linear trends for each channel as a function of latitude. For TMT, a warming trend is present north of 42.5°S, with the strongest warming present in the northern high latitudes. South of 45.0°S, there is moderate cooling. For TLS, cooling is present at all latitudes, with the strongest cooling occurring at the midlatitudes. The TTS trends are, in general, a combination of the tropospheric and stratospheric trends, which tend to cancel each other. Near the poles, the variability of both the TTS and TLS channels is dominated by stratospheric warming events, which increases the estimated errors for the linear trends. In these areas, the TTS trends can appear to be inconsistent with the TMT and TLS trends. This is in part because the TTS trends are calculated over the shorter 1987–2006 period.

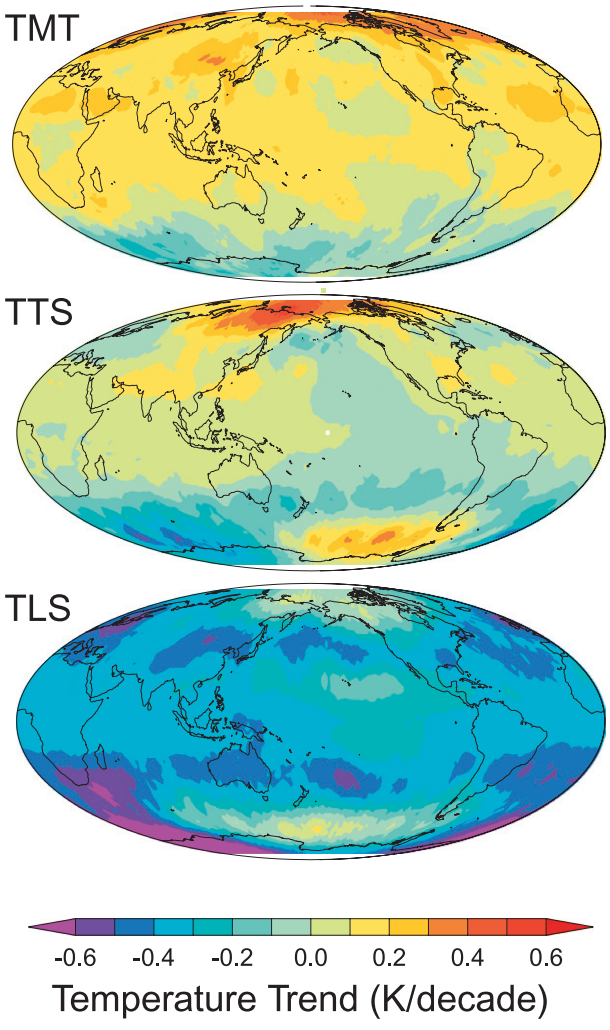

FIG. 12. Global maps of linear trends for each channel, calculated over the same time periods used in Fig. 11.

When the year-to-year variations in the stratospheric warming events dominate the long-term trends, the difference in trend period is important.

c. *Global maps of trends*

In Fig. 12, we show color-coded maps of trends for each channel. The TMT and TLS trends are shown for the longer 1979–2006 period whereas the TTS trends are for 1987–2006. The TMT trends are mostly positive, with the largest in the northern polar regions, particularly in the Canadian Arctic. The TTS trends are both positive and negative, with the largest positive trends in the Arctic. The largest negative trends are over the southern Indian and Atlantic Oceans, with positive trends over large areas of the South Pacific. The TLS trends are mostly negative, with the largest cooling trends over the southern Indian and Atlantic Oceans and over the Antarctic continent.

6. Conclusions

In this work we have described the methods used to combine measurements from MSU and AMSU microwave sounders into three long-term datasets. We have made significant efforts to ensure that the long-term calibration is as stable as possible because the intended use of these datasets is to evaluate decadal climate change and to test climate model results on multidecadal time scales. The results of this work are freely available online (versions 3.2; http://www.remss.com/msu/).

Acknowledgments. This work was supported by the NOAA Climate and Global Change Program Award NA05OAR4311111.

APPENDIX

Relationship Between Our Error Model and a Physically Based Error Model

Our error model [Eq. (5)] describes the relationship between the true brightness temperature T_0 and that measured by the satellite T:

$$T = T_0 + A + \alpha T_{\text{TARGET}} + \beta T_{\text{SCENE}} + \varepsilon. \quad \text{(A1)}$$

Here, A is a constant offset, and α and β are, respectively, the target factor and the "scene factor" that describe the dependence of the error on the calibration target temperature T_{TARGET} and the scene temperature T_{SCENE}. Both these terms are expected if the calibration error is due to either residual nonlinearity in the radiometer or to an error in the measurement of the calibration target temperature. This can be seen by comparing our error model to the physical error model introduced by Grody et al. (2004) and noting that Eq. (A1) represents an alternate linearization of the general model derived there. Grody et al. introduced two factors to account for errors in the hot and cold calibration temperatures (ΔT_{TARGET} and ΔT_{SPACE}) and for errors due to nonlinearity in the instrument calibration curve. For errors in the calibration temperatures, the error in the derived brightness temperature is given by

$$\Delta T = K\Delta T_{\text{TARGET}} + (1 - K)\Delta T_{\text{SPACE}},$$
$$K = \frac{T_{\text{SCENE}} - T_{\text{SPACE}}}{T_{\text{TARGET}} - T_{\text{SPACE}}}. \quad \text{(A2)}$$

The error due to nonlinearity is given by

$$\Delta T = \Delta\mu Z,$$
$$Z = (T_{\mathrm{SCENE}} - T_{\mathrm{SPACE}})(T_{\mathrm{TARGET}} - T_{\mathrm{SCENE}}), \tag{A3}$$

where $\Delta\mu$ is a parameter characterizing the deviation from linearity, which Grody et al. assumed to be quadratic. The resulting calibration equation is

$$T = T_0 + K\Delta T_{\mathrm{TARGET}} + (1 - K)\Delta T_{\mathrm{SPACE}} - Z\Delta\mu, \tag{A4}$$

where T_0 is the error-free temperature; T is the temperature obtained using the linear calibration equation; $\Delta T_{\mathrm{TARGET}}$, $\Delta T_{\mathrm{SPACE}}$, and $\Delta\mu$ are constants to be determined; and K and Z are functions of the observed brightness temperature and the temperature of the cold and hot calibration sources, respectively. Grody et al. noted that the K and Z factors are highly correlated and simplified their method by collapsing the data onto a linear relationship between K and Z using linear regression.

Here we propose an alternative procedure that separately linearizes the model for errors due to changes in T_{SCENE} and T_{TARGET} (we assume T_{SPACE} is fixed). By doing this, we retain the physical basis of the Grody et al. error model while producing an error model that is directly connected to measured temperatures. To begin, we perform a Taylor expansion of Eq. (A4) with respect to changes in T_{SCENE} and T_{TARGET} and retain only the linear terms:

$$T = T_0 + \Delta T_{\mathrm{SPACE}} + (\Delta T_{\mathrm{TARGET}} - \Delta T_{\mathrm{SPACE}})\left(K_0 + \frac{\partial K}{\partial T_{\mathrm{SCENE}}}\delta T_{\mathrm{SCENE}} + \frac{\partial K}{\partial T_{\mathrm{TARGET}}}\delta T_{\mathrm{TARGET}} + \ldots\right)$$
$$- \Delta\mu\left(Z_0 + \frac{\partial Z}{\partial T_{\mathrm{SCENE}}}\delta T_{\mathrm{SCENE}} + \frac{\partial Z}{\partial T_{\mathrm{TARGET}}}\delta T_{\mathrm{TARGET}} + \ldots\right). \tag{A5}$$

Collecting terms and rearranging yields

$$T = T + \Delta T_{\mathrm{SPACE}} + K_0(\Delta T_{\mathrm{TARGET}} - \Delta T_{\mathrm{SPACE}}) - Z_0\Delta\mu + \left[(\Delta T_{\mathrm{TARGET}} - \Delta T_{\mathrm{SPACE}})\frac{\partial K}{\partial T_{\mathrm{TARGET}}}\right.$$
$$\left. -\Delta\mu\frac{\partial Z}{\partial T_{\mathrm{TARGET}}}\right]\delta T_{\mathrm{TARGET}} + \left[(\Delta T_{\mathrm{TARGET}} - \Delta T_{\mathrm{SPACE}})\frac{\partial K}{\partial T_{\mathrm{SCENE}}} - \Delta\mu\frac{\partial Z}{\partial T_{\mathrm{SCENE}}}\right]\delta T_{\mathrm{SCENE}} + \ldots. \tag{A6}$$

or

$$T = T + A + \alpha\delta T_{\mathrm{TARGET}} + \beta\delta T_{\mathrm{SCENE}} + \text{higher-order terms}. \tag{A7}$$

Note that the first-order terms in Eq. (A7) are the same as in Eq. (A1). The constants A, α, and β are given by

$$A = \Delta T_{\mathrm{SPACE}} + K_0(\Delta T_{\mathrm{TARGET}} - \Delta T_{\mathrm{SPACE}}) - Z_0\Delta\mu,$$
$$\alpha = \left[(\Delta T_{\mathrm{TARGET}} - \Delta T_{\mathrm{SPACE}})\frac{\partial K}{\partial T_{\mathrm{TARGET}}} - \Delta\mu\frac{\partial Z}{\partial T_{\mathrm{TARGET}}}\right], \quad \text{and}$$
$$\beta = \left[(\Delta T_{\mathrm{TARGET}} - \Delta T_{\mathrm{SPACE}})\frac{\partial K}{\partial T_{\mathrm{SCENE}}} - \Delta\mu\frac{\partial Z}{\partial T_{\mathrm{SCENE}}}\right], \tag{A8}$$

where the partial derivatives are evaluated at the typical values for T_{SPACE}, T_{TARGET}, and T_{SCENE}. The first three terms in Eq. (A7) correspond to the empirical error model originally developed by Christy et al. (2000) and also used by Mears et al. (2003) and Mears and Wentz (2005).

REFERENCES

Christy, J. R., R. W. Spencer, and W. D. Braswell, 2000: MSU tropospheric temperatures: Dataset construction and radiosonde comparisons. *J. Atmos. Oceanic Technol.,* **17,** 1153–1170.

——, ——, W. B. Norris, W. D. Braswell, and D. E. Parker, 2003: Error estimates of version 5.0 of MSU–AMSU bulk atmospheric temperatures. *J. Atmos. Oceanic Technol.,* **20,** 613–629.

Dai, A., and K. E. Trenberth, 2004: The diurnal cycle and its depiction in the community climate system model. *J. Climate,* **17,** 930–951.

Fu, Q., and C. M. Johanson, 2005: Satellite-derived vertical dependence of tropospheric temperature trends. *Geophys. Res. Lett.,* **32,** L10703, doi:10.1029/2004GL022266.

——, ——, S. G. Warren, and D. J. Seidel, 2004: Contribution of stratospheric cooling to satellite-inferred tropospheric temperature trends. *Nature,* **429,** 55–58.

Goodrum, G., K. B. Kidwell, and W. Winston, cited 2000: NOAA KLM user's guide. National Climatic Data Center. [Available online at http://www2.ncdc.noaa.gov/docs/klm/index.htm.]

Grody, N. C., K. Y. Vinnikov, M. D. Goldberg, J. T. Sullivan, and J. D. Tarpley, 2004: Calibration of multisatellite observations for climatic studies: Microwave sounding unit (MSU). *J. Geophys. Res.,* **109,** D24104, doi:10.1029/2004JD005079.

Ho, S.-P., Y.-H. Kuo, Z. Zeng, and T. C. Peterson, 2007: A comparison of lower stratosphere temperature from microwave measurements with CHAMP GPS RO data. *Geophys. Res. Lett.,* **34,** L15701, doi:10.1029/2007GL030202.

Kalnay, E., and Coauthors, 1996: The NCEP/NCAR 40-Year Reanalysis Project. *Bull. Amer. Meteor. Soc.,* **77,** 437–471.

Kidwell, K. B., cited 1998: NOAA polar orbiter data users guide. National Climatic Data Center. [Available online at http://www.ncdc.noaa.gov/oa/pod-guide/ncdc/docs/podug/index.htm.]

Kiehl, J. T., J. J. Hack, G. B. Bonan, B. A. Boville, B. P. Briegleb, D. L. Williamson, and P. J. Rasch, 1996: Description of the NCAR Community Climate Model (CCM3). NCAR Tech. Rep. NCAR/TN-420+STR, 152 pp.

Lanzante, J. R., S. Klein, and D. J. Seidel, 2003: Temporal homogenization of monthly radiosonde temperature data. Part II: Trends, sensitivities, and MSU comparison. *J. Climate,* **16,** 241–262.

Mears, C. A., and F. J. Wentz, 2005: The effect of drifting measurement time on satellite-derived lower tropospheric temperature. *Science,* **309,** 1548–1551.

——, M. C. Schabel, F. J. Wentz, B. D. Santer, and B. Govindasamy, 2002: Correcting the MSU middle tropospheric temperature for diurnal drifts. *Proc. Int. Geophysics and Remote Sensing Symp.,* Vol. III, Toronto, ON, Canada, IEEE, 1839–1841.

——, ——, and ——, 2003: A reanalysis of the MSU channel 2 tropospheric temperature record. *J. Climate,* **16,** 3650–3664.

Prabhakara, C., R. Iaacovazzi, J.-M. Yoo, and G. Dalu, 2000: Global warming: Evidence from satellite observations. *Geophys. Res. Lett.,* **27,** 3517–3520.

Prigent, C., J. P. Wigneron, W. B. Rossow, and J. R. Pardo-Carrion, 2000: Frequency and angular variations of land surface microwave emissivities: Can we estimate SSM/T and AMSU emissivities from SSM/I emissivities? *IEEE Trans. Geosci. Remote Sens.,* **38,** 2373–2386.

Randel, W. J., and F. Wu, 2006: Biases in stratospheric and tropospheric temperature trends derived from historical radiosonde data. *J. Climate,* **19,** 2094–2104.

Rosenkranz, P., 1993: Absorption of microwaves by atmospheric gases. *Atmospheric Remote Sensing by Microwave Radiometry,* Michael A. Janssen, Ed., John Wiley and Sons, 37–90.

——, 1998: Water vapor microwave continuum absorption: A comparison of measurements and models. *Radio Sci.,* **33,** 919–928.

Seidel, D. J., and Coauthors, 2004: Uncertainty in signals of large-scale climate variations in radiosonde and satellite upper-air temperature datasets. *J. Climate,* **17,** 2225–2240.

Sherwood, S., J. R. Lanzante, and C. Meyer, 2005: Radiosonde daytime biases and late 20th-century warming. *Science,* **309,** 1556–1559.

Spencer, R. W., and J. R. Christy, 1992: Precision and radiosonde validation of satellite gridpoint temperature anomalies. Part II: A tropospheric retrieval and trends during 1979–1990. *J. Climate,* **5,** 858–866.

Ulaby, F. T., R. K. Moore, and A. K. Fung, 1981: *Microwave Remote Sensing: Active and Passive*. Vol. 1, *Microwave Remote Sensing Fundamentals and Radiometry,* Artech House, 456 pp.

Vinnikov, K. Y., N. C. Grody, A. Robock, R. J. Stouffer, P. D. Jones, and M. D. Goldberg, 2005: Temperature trends at the surface and in the troposphere. *J. Geophys. Res.,* **111,** D03106, doi:10.1029/2005JD006392.

Wentz, F. J., and T. Meissner, 2000: AMSR ocean algorithm: Algorithm theoretical basis, version 2. Remote Sensing Systems Doc. 121599A-1, 66 pp.

Zou, C.-Z., M. D. Goldberg, Z. Cheng, N. C. Grody, J. T. Sullivan, C. Cao, and D. Tarpley, 2006: Recalibration of microwave sounding unit for climate studies using simultaneous Nadir overpasses. *J. Geophys. Res.,* **111,** D19114, doi:10.1029/2005JD006798.